The Astrophysical Journal, 979:19 (12pp), 2025 January 20 https://doi.org/10.3847/1538-4357/ad9c7a

Line List for the $A^2\Pi-X^2\Sigma^+$ and the $B^2\Sigma^+-X^2\Sigma^+$ Band Systems of CaF

Léo Lavy[1,3], Peter F Bernath[1,2], and Adam Pastorek[1]
[1] Department of Chemistry and Biochemistry, Old Dominion University, Norfolk, VA 23529, USA
[2] Department of Physics, Old Dominion University, Norfolk, VA 23529, USA
Received 2024 November 11; revised 2024 December 3; accepted 2024 December 5; published 2025 January 15

Abstract

The spectral analysis of molecule-rich asymptotic giant branch (AGB) stars is challenging. Although other calcium and fluorine bearing molecules are observed in the microwave and in the visible spectrum of AGB stars, CaF has never been detected, despite favorable chemical equilibrium predictions. Yet, measuring the CaF abundance could give more insight into the fluorine budget of AGB stars and allow better simulation of stellar spectra. In this work, we present an analysis of the visible spectrum of CaF obtained with a Fourier transform spectrometer. CaF $A^2\Pi-X^2\Sigma^+$ and $B^2\Sigma^+-X^2\Sigma^+$ band systems were excited with a hollow cathode discharge. Using previous fluorescence spectroscopy measurements, highly accurate ground state constants, and reasonable extrapolation schemes, the strongest features of CaF in the visible spectrum can be accurately modeled for both band systems. Spectroscopic constants are determined for $A^2\,\Pi$ with $v \leqslant 16$ and for $B^2\Sigma^+$ with $v \leqslant 20$. Ab initio transition dipole moment curves of both transitions were calculated and scaled, and we provide a line list with Einstein A coefficients and oscillator strengths. This line list can be used to simulate spectra of CaF at temperatures and pressures relevant to astrophysical environments.

Unified Astronomy Thesaurus concepts: Spectral line lists (2082); Laboratory astrophysics (2004); Molecular spectroscopy (2095); Molecular spectroscopic constants (2260)

Materials only available in the online version of record: machine-readable tables

1. Introduction

Asymptotic giant branch (AGB) stars are the late stage of evolution of low- and intermediate-mass stars ($<8\,M_\odot$). While burning helium in their core, these stars have a large radius and their atmosphere is relatively cool, ranging from 2000 to 3000 K. This cool atmosphere is favorable for the formation of molecules that are observed in the visible region. The elements found in cool stellar atmospheres are often similar to those found in the Sun, i.e., an M-type star with a carbon to oxygen ratio (C/O) of ~0.54. The elemental abundance is changed during dredge-ups that bring s-process elements and elemental carbon to the surface; therefore, the spectral type of AGB stars typically evolves from M-type to S-type (C/O ~ 1), and then to C-type (C/O > 1). The difference between these spectral types is linked to the C/O ratio with insight given by chemical equilibrium models (M. Agúndez et al. 2020): the highly stable CO molecule traps most of the excess C and O atoms. As a result, the strongest bands in the M-type stellar spectra belong to TiO and VO, in S-type stars to ZrO, and in C-type stars to CN and C_2.

The abundance of calcium in AGB atmospheres is similar to that in the Sun's photosphere, that is $\sim 2 \times 10^{-6}$ atoms of calcium per one atom of hydrogen ($\log \epsilon = 6.34$; M. Asplund et al. 2009). At chemical equilibrium, most of the calcium exists in the form of neutral atoms and some is trapped into molecules such as CaCl and CaF. CaCl is observed to be a strong absorption feature in the visible spectrum of some S- and C-type stars (R. Clegg & S. Wyckoff 1977). CaC_2 was recently observed in the microwave toward the envelope of the C-star IRC+10216 (H. Gupta et al. 2024). In this same star, a CaF signal was sought decades ago in the microwave region without success (L. M. Ziurys et al. 1994). Yet CaF is more stable than CaCl with a dissociation energy of $D_{0,\mathrm{CaF}} = 5.48$ eV (Y.-R. Luo 2007) versus $D_{0,\mathrm{CaCl}} = 4.20$ eV (J. Rumble 2023), and, according to chemical equilibrium calculations, CaF exists in M-type (O-rich) stars with a molar fraction only two times less than CaCl (M. Agúndez et al. 2020). Note also that the $\tilde{A}^2\Pi - \tilde{X}^2\Sigma^+$ and $\tilde{B}^2\Sigma^+ - \tilde{X}^2\Sigma^+$ transitions of the isovalent CaOH molecule have been observed in M dwarf stars (A. S. Rajpurohit et al. 2013), and line lists have recently been provided (A. Owens et al. 2022).

Solar fluorine abundance is about 10 times lower than that of chlorine; however, a significant over-abundance of fluorine has been reported in AGB stars due to its synthesis during helium shell flashes (A. Jorissen et al. 1992; K. Werner et al. 2005). Overall, the cosmic origin of fluorine remains uncertain and AGB stars could play a significant role in its production. In AGB atmospheres, a considerable amount of fluorine is locked in the AlF and HF molecules. AlF was observed in the microwave spectral range by Atacama Large Millimeter/submillimeter Array (M. Saberi et al. 2022) and Caltech Submillimeter Observatory (L. M. Ziurys et al. 1994), for example. The observation of new F-bearing species such as CaF can provide a better view of the fluorine budget in AGB stars.

Because of the high electronegativity of fluorine, the electronic structure of CaF is mainly ionic (Ca^+F^-) with the unpaired electron located on the calcium atom. The excitation of this solitary electron generates the lowest electronic states of the molecule: $X^2\Sigma^+$, $A^2\Pi$, and $B^2\Sigma^+$. The resulting band systems $A^2\Pi-X^2\Sigma^+$ and $B^2\Sigma^+-X^2\Sigma^+$ are in the visible region.

[3] Corresponding author.

Table 1
Sample of Lines and Residuals for the Ground State Constants

F'	p'	F''	p''	Obs (MHz)	Calc (MHz)	$O-C$ (MHz)	StdDev	Line Assignment
3	f	2	f	82117.4753	82117.4829	−0.0076	0.003	rR2(2.5)3,2: $X\ v=0$ 3.5 4 F2f 3–$X\ v=0$ 2.5 3 F2f 2: Anderson1994
4	e	3	e	82120.4165	82120.3458	0.0707	0.003	rR2(2.5)4,3: $X\ v=0$ 3.5 4 F2f 4–$X\ v=0$ 2.5 3 F2f 3: Anderson1994
4	e	3	e	82152.9974	82153.0268	−0.0294	0.003	rR1(3.5)4,3: $X\ v=0$ 4.5 4 F1e 4–$X\ v=0$ 3.5 3 F1e 3: Anderson1994
5	f	4	f	82156.2594	82156.2514	0.008	0.003	rR1(3.5)5,4: $X\ v=0$ 4.5 4 F1e 5–$X\ v=0$ 3.5 3 F1e 4: Anderson1994
4	f	3	f	102648.8844	102648.8766	0.0078	0.003	rR2(3.5)4,3: $X\ v=0$ 4.5 5 F2f 4–$X\ v=0$ 3.5 4 F2f 3: Anderson1994

Note. F' and F'' are the total angular momenta of upper and lower states, respectively; p' and p'' are the parity of upper and lower states, respectively; Obs is the observed line position in MHz, Calc is the calculated line position in MHz, and $O-C$ is the observed minus calculated line position in MHz. StdDev is the inverse of the weight for this line used in the fit. The line assignment shows first the branch name, then the upper state ($X^2\Sigma^+ v = 0$ in this case), followed by J', N', its spin component (F1 or F2), its parity excluding hyperfine structure (f or e), F', and the same for the lower state after the dash character. The reference of the line assignment is indicated after a colon: Anderson1994 refers to M. A. Anderson et al. (1994), ChildsGoodman1981 refers to W. Childs et al. (1981), Weiler1986 refers to G. Weiler (1986), and Charron1995 refers to F. Charron et al. (1995).

(This table is available in its entirety in machine-readable form in the online article.)

The A–X band system was studied in several laser-induced fluorescence experiments: by R. W. Field et al. (1975), J. Nakagawa et al. (1978), and more recently by L. A. Kaledin et al. (1999) for $v = 0$–2. Hyperfine structure of the A state was measured (P. Bernath et al. 1980) but it is not resolved in the visible region. The A–X transition has interesting properties for laser cooling experiments; in fact, CaF was one of the first molecules to be laser cooled (V. Zhelyazkova et al. 2014). The B–X band system was studied by M. Dulick et al. (1980) with assignments up to $v = 15$ and by L. A. Kaledin et al. (1999) by laser-induced fluorescence spectroscopy. The ground state X of CaF was thoroughly studied experimentally: infrared bands with $\Delta v = \pm 1$ were measured up to $v = 8$ by F. Charron et al. (1995). For the first few vibrational quantum numbers, W. Childs et al. (1981) measured hyperfine transitions, G. Weiler (1986) measured forbidden transitions, and M. A. Anderson et al. (1994) measured pure rotational transitions. Recently, the X state was also studied theoretically (S. Hou & P. F. Bernath 2018).

Future ground-based "extremely large telescopes" will provide higher resolution spectra of stars in the visible region, e.g., The Thirty Meter Telescope (W. Skidmore 2015). With these measurements there is a reasonable chance that new molecules will be discovered. A better knowledge of the CaF spectrum could be the key to its detection. A detailed line list of CaF would also be useful for modeling and interpreting the spectra of stars in the context of exoplanetary research (J. Tennyson & S. N. Yurchenko 2012). While previous laboratory studies excited CaF with a laser in fluorescence-induced experiments, current knowledge allows an analysis of thermally excited CaF. A hollow cathode discharge excites many vibrational bands of CaF that are relevant for astrophysical observations; generally, the vibrational temperature is very high in the hollow cathode spectrum, similar to the temperature in AGB atmospheres. In this study, we present a thorough analysis of a CaF spectrum excited in a hollow cathode experiment and measured by use of a Fourier transform spectrometer. Nearly all the observed vibrational bands are analyzed despite the high density of lines in the spectrum. In the first section, the methods detailing our experiment, and computational and fitting procedures, are presented. The results are then provided with an overview of the spectrum, the calculation of the equilibrium constants, and the calculation of line strengths. A final section compares the present CaF results with the similar CaCl system and the implications for the detection of these molecules in stars.

2. Methods

2.1. Experimental Setup

The hollow cathode has been prepared by pressing a finely ground mixture of copper powder (11 g) and calcium fluoride (1.5 g) with a pellet press into a copper cathode body. Subsequently, a hole was drilled through the pressed mixture to create a ~1 mm thin layer on the cathode wall. The cathode was sputtered using a constant flow of argon buffer gas (1 Torr) while evacuating the sample space. An electric current of 0.4 A and a voltage of 540 V were measured during the discharge. The spectrometer was set with an entrance aperture of 1.7 mm, a resolution of 0.05 cm^{-1}, and an observation window of 9000–25,000 cm^{-1}. A quartz visible beamsplitter was used, with the rest of the optics made from CaF_2. The spectra were detected by use of a Si-photodiode detector and 800 scans were averaged to obtain a reasonable signal-to-noise ratio (SNR). The laboratory wavenumber scale was calibrated using 28 standard Ar II lines originally proposed by R. C. M. Learner & A. P. Thorne (1988) and remeasured by W. Whaling et al. (1995), specifically for a hollow cathode. Among these lines, 26 were within the range of the experimental spectrum. A scaling factor of 1.00000017702 was obtained and applied to the observed wavenumbers.

2.2. Ab Initio Calculations

Transition dipole moment (TDM) curves were calculated with the MOLPRO, version 2012.1, quantum chemistry package (H. Werner et al. 2011; H.-J. Werner et al. 2020, 2022) using the internally contracted multireference configuration interaction method (MRCI; H.-J. Werner & P. J. Knowles 1988). State-averaged complete active space self-consistent field calculations (CASSCF; H.-J. Werner & P. J. Knowles 1985; D. A. Kreplin et al. 2019) were performed to optimize the molecular orbitals (MOs) used in the MRCI calculations. Two CASSCF calculations were made, one for each transition. The correlation consistent basis set cc-pVQZ (J. G. Hill & K. A. Peterson 2017) was used for the calcium atom, and aug-cc-pVQZ (R. A. Kendall et al. 1992) for the fluorine atom. In the CASSCF calculations, six orbitals belonging to A_1 representation, 2 B_1, 2 B_2, and 0 A_2 were

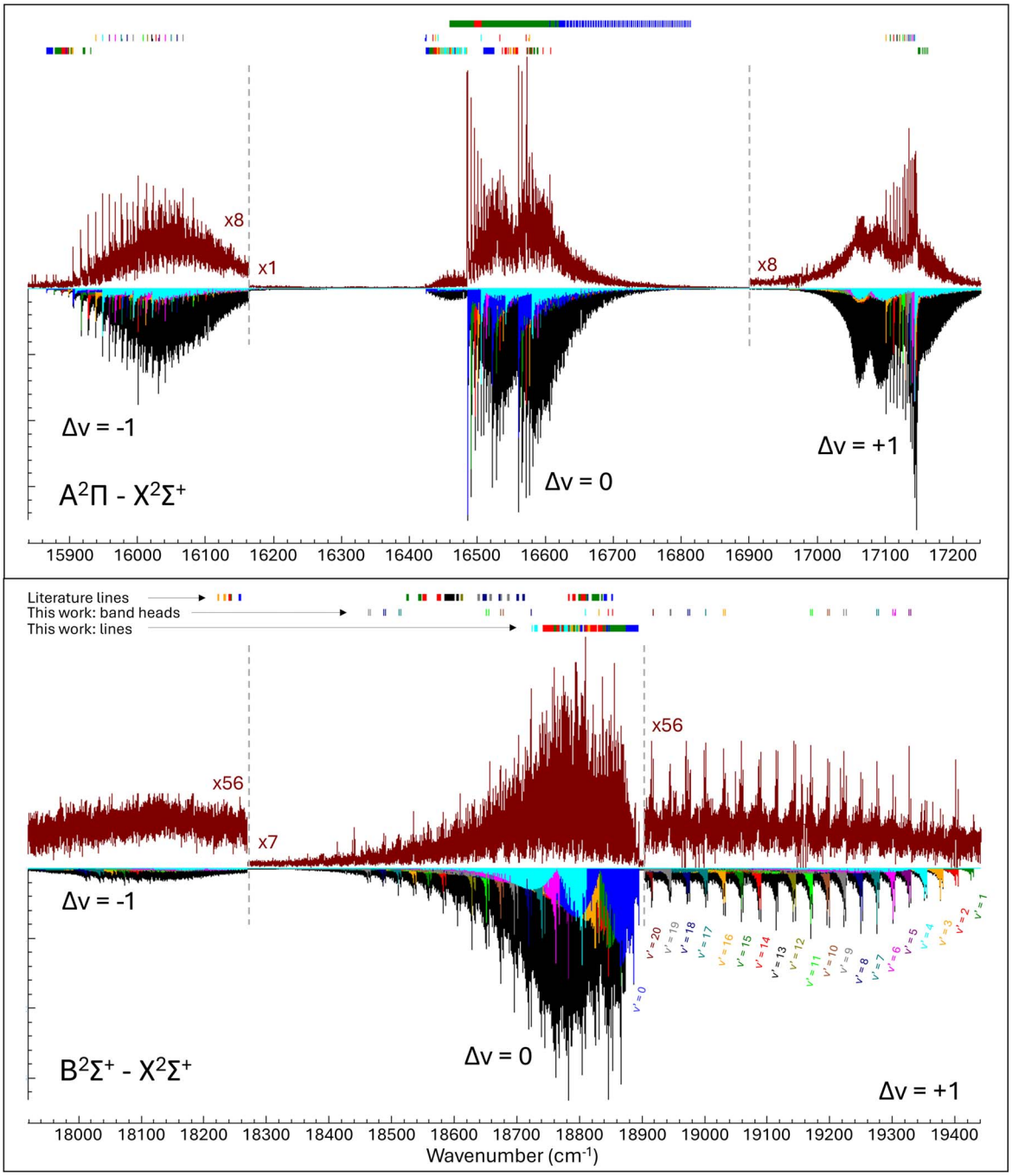

Figure 1. Experimental hollow cathode spectrum of CaF (upward) and fit from this work (downward). The total fit is in black and the colors correspond to individual upper state vibrational quantum number v'. Vertical lines at the top of the spectrum show the assignments used in this work, from top to bottom: literature lines, band head assignments from this work, and line assignments from this work. For the total fit, the simulation uses a rotational temperature of 2500 K and a vibrational temperature of 4000 K with a Gaussian line width of 0.08 cm^{-1}.

doubly occupied in all configurations, corresponding to Ca 1*s*, 2*s*, 2*p*, 3*s*, $3p_x$, $3p_y$, and F 1*s*, 2*s* atomic orbitals. The active space consists of 9 electrons in 10 MOs (5 A_1, 2 B_1, 2 B_2, 1 A_2) involving Ca $3p_z$, 4*s*, $3d_{z^2}$, $3d_{xz}$, $3d_{yz}$, and F 2*p*, 3*s*, $3d_{xy}$ atomic orbitals. In the MRCI calculations the same active space was used but excitations from the fluorine 2*s* and Ca 3*p* orbitals were allowed. The *A*–*X* TDM curve calculated in this work is in excellent agreement with the curve calculated by M. Pelegrini et al. (2005). Moreover, the values of the *A*–*X* and *B*–*X* TDMs at the equilibrium bond length are in agreement with Y. Hao et al.(2019).

2.3. Spectral Fitting

The transitions were rotationally analyzed using PGOPHER (C. M. Western 2017). PGOPHER uses the standard N^2 Hamiltonian, where N is the rotational angular momentum excluding electron spin ($N = J - S$). The Hamiltonian is described in detail elsewhere (J. M. Brown & A. Carrington 2003). Briefly, the Hamilonian matrix is constructed in the basis of e/f parity basis functions (P. F. Bernath 2020) using vibrational effective parameters. Here, the relevant parameters (in reciprocal centimeters, cm^{-1}) are the origin T_v, the rotational constant B_v (with centrifugal distortion parameters

Table 2
Sample of Lines and Residuals for the Excited State Constants

J'	J''	Obs (cm^{-1})	Calc (cm^{-1})	$O-C$	Line Assignment
125.5	124.5	18831.5437	18831.5294	0.0143	rR2(124.5): B $v=3$ 125.5 126 F2f–X $v=3$ 124.5 125 F2f: ThisWorkBandHead
126.5	125.5	18831.5437	18831.4930	0.0508	rR2(125.5): B $v=3$ 126.5 127 F2f–X $v=3$ 125.5 126 F2f: ThisWorkBandHead
66.5	67.5	15867.0794	15867.0733	0.0061	oP12(67.5): A $v=0$ 66.5 66 F1f–X $v=1$ 67.5 68 F2f: ThisWork
65.5	66.5	15867.2731	15867.2689	0.0042	oP12(66.5): A $v=0$ 65.5 65 F1f–X $v=1$ 66.5 67 F2f: ThisWork
60.5	61.5	15868.4538	15868.4551	−0.0012	oP12(61.5): A $v=0$ 60.5 60 F1f–X $v=1$ 61.5 62 F2f: ThisWork

Note. J' and J'' are the total angular momenta of upper and lower states, respectively; Obs is the observed line position in reciprocal centimeters, Calc is the calculated line position in reciprocal centimeters, and $O-C$ is the observed minus calculated line position in reciprocal centimeters. The line assignment is presented similarly as in Table 1. The reference of the line assignment is indicated after a colon: ThisWorkBandHead and ThisWork refer to lines assigned in this work, Dulick1980 refers to lines from M. Dulick et al. (1980) in addition to those from Kaledin, Kaledin1999 refers to lines of A–X reported by L. A. Kaledin et al. (1999) (including lines from R. W. Field et al. 1975 and J. Nakagawa et al. 1978), and Kaledin1999B refers to lines of B–X reported by L. A. Kaledin et al. (1999) (including corrected lines of M. Dulick et al. 1980).

(This table is available in its entirety in machine-readable form in the online article.)

D_v and H_v), the spin–orbit coupling constant A_v (with centrifugal distortion parameter A_{Dv}), the spin–rotation coupling constant γ_v (with centrifugal distortion parameter γ_{Dv}), and the Λ-doubling parameters p_v (with centrifugal distortion parameter p_{Dv}) and q_v (with centrifugal distortion parameter q_{Dv}). The parameters b and c represent the coupling of electron spin S with nuclear spin I, and the parameter c_I represent the coupling of the nuclear spin with rotation.

The spectral fitting was performed in two steps. In the first step, the ground state spectroscopic constants were fitted, including the known hyperfine structure. The nuclear spin of ^{40}Ca is 0 and the nuclear spin of ^{19}F is 1/2, therefore, every line splits into two hyperfine components. Lines from the literature are gathered in Table 1; these include infrared bands with $\Delta v = \pm 1$ measured up to $v = 8$ by F. Charron et al. (1995), pure rotational transitions measured by M. A. Anderson et al. (1994) for $v = 0$–4, fine and hyperfine transitions measured by W. Childs et al. (1981) for $v = 0$–3, and forbidden transitions measured by G. Weiler (1986) for $v = 0$. Note that when no hyperfine lines were reported, both hyperfine components are assigned to the observed unresolved value. The line weights were set according to the standard deviation of the observed line. For the ground states of $v = 0, 1$, nearly all of the constants are reoptimized. For $v \leqslant 8$, the constants of M. A. Anderson et al. (1994) were used when available, or those of F. Charron et al. (1995) if otherwise. We fitted H_v, γ_v, γ_{Dv}, and the hyperfine parameter b for $v \leqslant 4$. For $v > 4$, no hyperfine data exist to our knowledge so the values were fixed. As shown by the residuals ($O-C$) in Table 1, the resulting set of constants reproduces the observed line positions very well.

In a second step, the ground state constants were fixed with hyperfine splitting removed and the excited state constants were optimized. For the fitting of the excited states, a set of lines from the literature, lines assigned in this work, and band heads assigned in this work belonging to the A–X and B–X band systems were used. These lines are shown in Figure 1 and are listed in Table 2.

For the A–X system, literature lines include measurements from L. A. Kaledin et al. (1999) and references therein. Assignments of this work consist of lines in the $^{o}P_{12}$ branch[4] in the $\Delta v = -1$, 0 sequences with $v' \leqslant 4$ and some lines with $\Delta v = 0$ and $v' \leqslant 3$ in the $^{q}Q_1$ and $^{q}Q_2$ branches. The $\Omega = 3/2$ spin component[5] was so blended that very few line assignments could be made. However, the band heads were assigned up to $v' = 16$ in the $\Delta v = +1$ sequence. The $\Omega = 1/2$ spin component $^{p}Q_{12}$ band heads were assigned up to $v' = 9$ in the $\Delta v = -1$ sequence. Table 3 shows the result of the fit. The spectroscopic constants T_v and B_v from $v' = 0$ to $v' = 16$ were fitted. A_v was fitted when band heads from both spin components were observed. D_v was fitted only for $v' = 0$–2. Many constants were kept fixed during the fit, either by taking the value for $v' = 0$ or extrapolating from fitted parameters.

For the B–X system, literature lines from L. A. Kaledin et al. (1999) and measurements from M. Dulick et al. (1980) were added, containing $\Delta v = -1$ lines with $v' \leqslant 4$ and lines from the (8, 8), (9, 9), (12, 12), (13, 13), (14, 14), and (15, 15) bands. The lines of M. Dulick et al. (1980) were corrected by a subtraction of 0.0056 cm^{-1} as suggested by S. Gerstenkorn & P. Luc (1979). All line assignments in this work were made in the $\Delta v = 0$ sequence. These consisted of $^{p}P_1$, $^{p}P_2$, $^{r}R_1$, and $^{r}R_2$ branches with $v' \leqslant 4$. When no lines were available from the literature, $^{r}R_1$ and $^{r}R_2$ band heads were assigned in the $\Delta v = +1$ sequence up to $v' = 20$, and some of those also in the $\Delta v = 0$ sequence. Table 3 shows the result of the fit. The spectroscopic constants T_v and γ_v were fitted when observations of M. Dulick et al. (1980) were available. B_v was fitted from $v' = 0 - 20$, and D_v was fitted only for v'=0–3, 8–9. Overall, the B–X band system is better characterized than the A–X band system.

3. Results

3.1. Spectrum Overview

Figure 1 shows an overview of the A–X and B–X band systems observed in the hollow cathode experiment (upward), and of the simulated spectrum from this work (downward). Atomic lines have been removed from the experimental spectrum. Individual observations reported in Table 2 are shown as vertical lines at the top of the spectrum. The strongest signal is obtained for A–X, the strongest bands correspond to $\Delta v = 0$ and the bands with $\Delta v = \pm 1$, about eight times weaker, are scaled for visibility. The spin components are widely separated, showing that the $A^2\Pi$ excited state follows Hund's case (a) coupling. The lower wavenumber component

[4] Branch notation: $^{\Delta N}\Delta J_{F'F''}$ where F is the spin component here (either $F1$ or $F2$) and redundancy is removed if $F' = F''$.

[5] Ω is the projection of J along the internuclear axis.

Table 3
CaF Spectroscopic Constants in Reciprocal Centimeters

$X^2\Sigma^{+a}$ spectroscopic constants and hyperfine constants										
v	T_v	B_v	$10^7 D_v$	$10^{15} H_v$	γ_v	$10^{11}\gamma_{Dv}$	b	c	$10^7 c_I$	
0	0	0.342488116(52)	4.68683(26)	−29.1(24)	0.00131747(59)	6.5(60)	0.003612(27)	0.00131(12)	9.7[b]	
1	582.84784(17)	0.340053826(53)	4.6899(14)[c]	−8.86(76)	0.00130724(93)	4(19)	0.003560(27)	0.00111[b]	9.7[b]	
2	1159.946892(192)[d]	0.337629458(70)[c]	4.6909(12)[c]	−4.41(64)	0.0012965(15)	−4(26)	0.003509(27)	0.00111[b]	9.7[b]	
3	1731.34856(21)[d]	0.335215314(80)[c]	4.6907(14)[c]	−6.75(49)	0.0012858(15)	−13(26)	0.003454(27)	0.00111[b]	9.7[b]	
4	2297.10325(27)[d]	0.332811563(112)[d]	4.69110(77)[d]	…	0.00127356(73)	…	0.003719[b]	0.00111[b]	9.7[b]	
5	2857.26144(37)[d]	0.330418358(181)[d]	4.69019(77)[d]	…	0.001263[e]	…	0.003719[b]	0.00111[b]	9.7[b]	
6	3411.87316(45)[d]	0.32803600(23)[d]	4.68889(76)[d]	…	0.001252[e]	…	0.003719[b]	0.00111[b]	9.7[b]	
7	3960.98951(61)[d]	0.32566419(35)[d]	4.68674(84)[d]	…	0.001241[e]	…	0.003719[b]	0.00111[b]	9.7[b]	
8	4504.65944(73)[d]	0.32330425(51)[d]	4.68533(98)[d]	…	0.001230[e]	…	0.003719[b]	0.00111[b]	9.7[b]	
9	5042.9334[e]	0.3209530[e]	4.6817[e]	…	0.001219[e]	…	…	…	…	
10	5575.8608[e]	0.3186130[e]	4.6781[e]	…	0.001208[e]	…	…	…	…	
11	6103.4912[e]	0.3162836[e]	4.6738[e]	…	0.001197[e]	…	…	…	…	
12	6625.8740[e]	0.3139648[e]	4.6689[e]	…	0.001186[e]	…	…	…	…	
13	7143.0582[e]	0.3116566[e]	4.6635[e]	…	0.001175[e]	…	…	…	…	
14	7655.0928[e]	0.3093589[e]	4.6574[e]	…	0.001164[e]	…	…	…	…	
15	8162.0267[e]	0.3070718[e]	4.6507[e]	…	0.001153[e]	…	…	…	…	
16	8663.9084[e]	0.3047953[e]	4.6434[e]	…	0.001142[e]	…	…	…	…	
17	9160.7866[e]	0.3025293[e]	4.6355[e]	…	0.001131[e]	…	…	…	…	
18	9652.7093[e]	0.3002739[e]	4.6270[e]	…	0.001120[e]	…	…	…	…	
19	10139.7249[e]	0.2980291[e]	4.6178[e]	…	0.001109[e]	…	…	…	…	

$A^2\Pi$ spectroscopic constants										
v	T_v	B_v	$10^7 D_v$	$10^{15} H_v$	A_v	A_{Dv}	p_v	$10^8 p_{Dv}$	q_v	$10^{10} q_{Dv}$
0	16528.7473(14)	0.3473918(13)	4.8017(18)	−53.7(83)	72.6135(28)	−0.0001744(29)	−0.04449(12)	−7.8(31)	−0.0002803(65)	7.8(25)
1	17117.2311(16)	0.3448679(19)	4.8137(43)	−16(25)	72.668(27)	−0.0001795(10)	−0.044856(40)	−7.8[f]	−0.0002785[e]	7.8[f]
2	17699.6538(40)	0.3423372(13)	4.81834(87)	…	72.7076(78)	−0.0001957(19)	−0.045403(96)	−7.8[f]	−0.000275(18)	7.8[f]
3	18275.9481(41)	0.33984641(49)	4.828[e]	…	72.7112(82)	−0.0001744[f]	−0.04582[e]	−7.8[f]	−0.0002724[e]	7.8[f]
4	18846.2887(43)	0.33735069(49)	4.836[e]	…	72.734(82)	−0.0001744[f]	−0.04628[e]	−7.8[f]	−0.0002698[e]	7.8[f]
5	19410.6827(66)	0.334853(46)	4.845[e]	…	72.7753(90)	−0.0001744[f]	−0.04674[e]	−7.8[f]	−0.0002671[e]	7.8[f]
6	19969.174(64)	0.3323563(42)	4.853[e]	…	72.8086(90)	−0.0001744[f]	−0.04719[e]	−7.8[f]	−0.0002645[e]	7.8[f]
7	20521.8639(66)	0.3298482(36)	4.861[e]	…	72.8443(87)	−0.0001744[f]	−0.04765[e]	−7.8[f]	−0.0002618[e]	7.8[f]
8	21068.6211(63)	0.3274152(35)	4.870[e]	…	72.870[e]	−0.0001744[f]	−0.04811[e]	−7.8[f]	−0.0002591[e]	7.8[f]
9	21609.7906(56)	0.324886(21)	4.878[e]	…	72.900[e]	−0.0001744[f]	−0.04857[e]	−7.8[f]	−0.0002565[e]	7.8[f]
10	22145.137(69)	0.322438(19)	4.886[e]	…	72.931[e]	−0.0001744[f]	−0.04902[e]	−7.8[f]	−0.0002538[e]	7.8[f]
11	22674.8497(92)	0.3199844(32)	4.895[e]	…	72.962[e]	−0.0001744[f]	−0.0495[e]	−7.8[f]	−0.0002511[e]	7.8[f]
12	23198.9067(95)	0.3175453(28)	4.903[e]	…	72.993[e]	−0.0001744[f]	−0.04994[e]	−7.8[f]	−0.0002485[e]	7.8[f]
13	23717.4214(88)	0.3151063(26)	4.911[e]	…	73.024[e]	−0.0001744[f]	−0.05040[e]	−7.8[f]	−0.0002458[e]	7.8[f]
14	24229.8384(80)	0.3127948(19)	4.920[e]	…	73.055[e]	−0.0001744[f]	−0.05085[e]	−7.8[f]	−0.0002431[e]	7.8[f]
15	24737.02(11)	0.31043(17)	4.928[e]	…	73.086[e]	−0.0001744[f]	−0.05131[e]	−7.8[f]	−0.0002405[e]	7.8[f]
16	25238.56(11)	0.308089(13)	4.936[e]	…	73.117[e]	−0.0001744[f]	−0.05177[e]	−7.8[f]	−0.0002378[e]	7.8[f]

$B^2\Sigma^+$ spectroscopic constants						
v	T_v	B_v	$10^7 D_v$	$10^{15} H_v$	γ_v	$10^8\gamma_{Dv}$
0	18833.1311(26)	0.3412892(19)	4.9003(34)	−120(16)	−0.045767(74)	−5.01(87)
1	19399.2844(24)	0.3386754(21)	4.9048(44)	−116(23)	−0.045942(81)	−6(11)
2	19959.2289(25)	0.3360826(14)	4.93361(82)	…	−0.046606(57)	…

Table 3
(Continued)

	$B^2\Sigma^+$ spectroscopic constants					
v	T_v	B_v	$10^7 D_v$	$10^{15} H_v$	γ_v	$10^8 \gamma_{Dv}$
3	20513.0322(53)	0.3334921(43)	4.9404(30)	…	−0.04701(25)	…
4	21060.7486[e]	0.33089528(49)	4.9302[e]	…	−0.04728[e]	…
5	21602.4363[e]	0.3283367(11)	4.9351[e]	…	−0.04767[e]	…
6	22138.1537[e]	0.3257748(11)	4.9400[e]	…	−0.04806[e]	…
7	22667.9589[e]	0.3232295(12)	4.9449[e]	…	−0.04846[e]	…
8	23191.9094(58)	0.3206916(45)	4.9456(45)	…	−0.04874(18)	…
9	23710.065(67)	0.318167(90)	4.952(22)	…	−0.04905(14)	…
10	24222.4817[e]	0.31565611(63)	4.9596[e]	…	−0.04963[e]	…
11	24729.2187[e]	0.31315992(66)	4.9645[e]	…	−0.05003[e]	…
12	25230.3347(68)	0.3106552(67)	4.9694[e]	…	−0.05035(30)	…
13	25725.885(32)	0.3081795(36)	4.9743[e]	…	−0.0509(21)	…
14	26215.9316(63)	0.3057075(87)	4.9792[e]	…	−0.05128(28)	…
15	26700.53(98)	0.303252(43)	4.9841[e]	…	−0.05165(61)	…
16	27179.7392[e]	0.300822(24)	4.989[e]	…	−0.05199[e]	…
17	27653.6169[e]	0.2984074(11)	4.9939[e]	…	−0.05239[e]	…
18	28122.2215[e]	0.2959775(12)	4.9988[e]	…	−0.05278[e]	…
19	28585.6109[e]	0.2935737(13)	5.0037[e]	…	−0.05317[e]	…
20	29043.8434[e]	0.2911775(42)	5.0086[e]	…	−0.05356[e]	…

Notes. One standard deviation is shown in parentheses.
[a] The constants of the ground state are optimized in a separate fit (see text).
[b] Fixed, values for $v = 0$ from M. A. Anderson et al. (1994).
[c] Fixed, values and standard deviation from M. A. Anderson et al. (1994).
[d] Fixed, values and standard deviation from F. Charron et al. (1995).
[e] Fixed, value obtained using equilibrium constants (see equations in the text and Table 4).
[f] Fixed, values for $v = 0$.

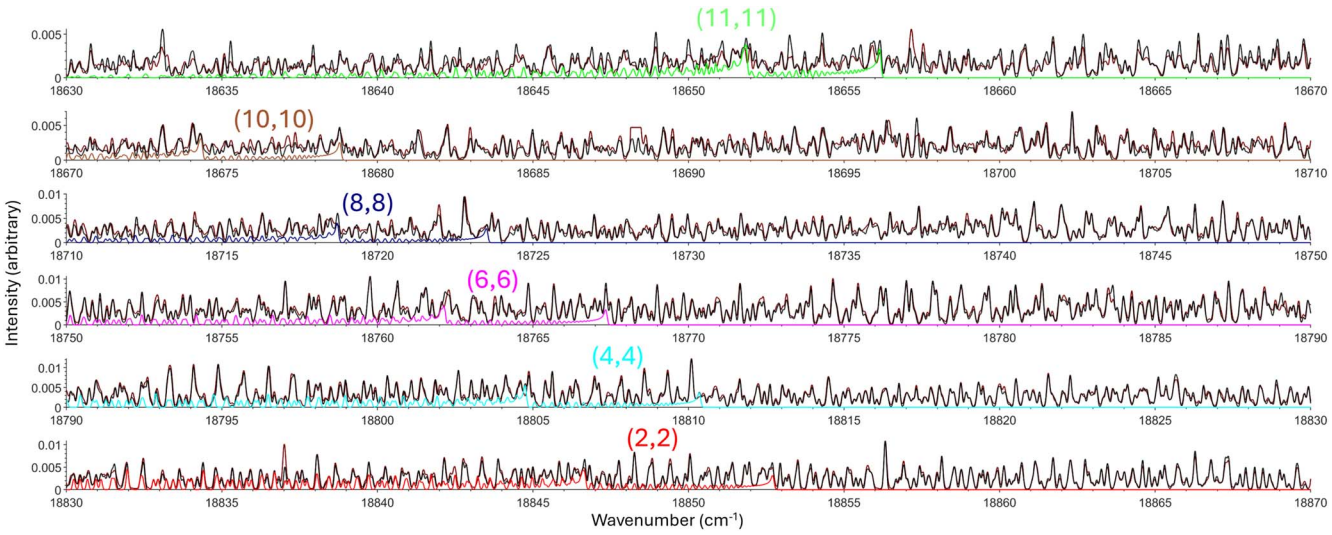

Figure 2. Sample of the experimental spectrum (brown) and the total fit (black) for the $B^2\Sigma^+ - X^2\Sigma^+$ band system between 18,630 and 18,870 cm^{-1}. Only some vibrational bands are shown in color for clarity.

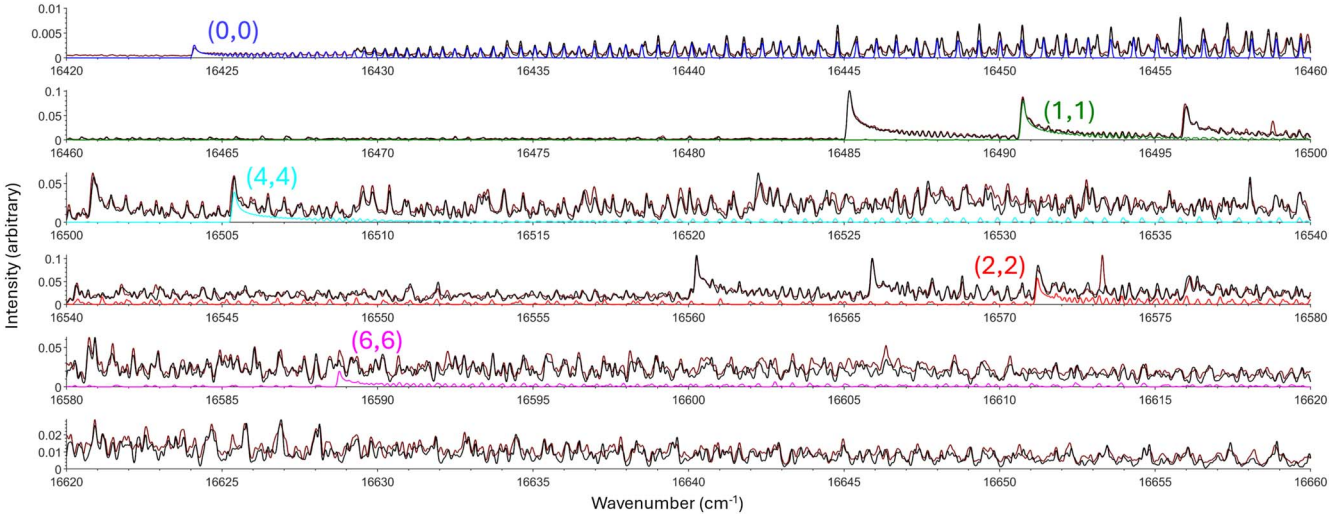

Figure 3. Sample of the experimental spectrum (brown) and the total fit (black) for the $A^2\Pi - X^2\Sigma^+$ band system between 16,420 and 16,660 cm^{-1}. Only some vibrational bands are shown in color for clarity.

corresponds to the $\Omega = 1/2$ spin component and the higher wavenumber component corresponds to $\Omega = 3/2$.

By using a rotational temperature of 2500 K, a vibrational temperature of 4000 K with a Gaussian line width of 0.08 cm^{-1} and the calculated band strengths (see Section 3.3), the simulation reproduces the strongest features ($\Delta v = 0$) of CaF remarkably well. Difficult regions remain: the $\Omega = 1/2$ spin component of A–X $\Delta v = +1$, where the interference of the many vibrational bands does not correspond to the experimental pattern, and the B–X $\Delta v = -1$ sequence, where the experimental SNR is too small. In the simulation, one can observe the very dense nature of the spectrum by comparing the total spectrum in black with individual vibrational bands in color.

Spectra with expanded x-axes for the $\Delta v = 0$ sequences of B–X and A–X spectra are presented in Figures 2 and 3, respectively. The agreement between the experimental spectrum (brown) and the simulated spectrum (black) is very good even for bands that were not investigated in previous works. Some vibrational bands are shown in color for guidance.

3.2. Equilibrium Constants

The spectroscopic constants of the vibronic states of $X^2\Sigma^+$, $A^2\Pi$, and $B^2\Sigma^+$ are presented in Table 3. The variation of the spectroscopic constants with respect to the vibrational quantum number v is fitted using the following polynomials, defining equilibrium constants:

$$T_v = T_e + \omega_e\left(v+\tfrac{1}{2}\right) - \omega_e x_e\left(v+\tfrac{1}{2}\right)^2 + \omega_e y_e\left(v+\tfrac{1}{2}\right)^3 + \omega_e z_e\left(v+\tfrac{1}{2}\right)^4, \quad (1)$$

$$B_v = B_e - \alpha_e\left(v+\frac{1}{2}\right) + \gamma_e\left(v+\frac{1}{2}\right)^2 + \epsilon_e\left(v+\frac{1}{2}\right)^3, \quad (2)$$

$$D_v = D_e + \beta_e\left(v+\frac{1}{2}\right), \quad (3)$$

$$A_v = A_e + \alpha_A\left(v+\frac{1}{2}\right) + \gamma_A\left(v+\frac{1}{2}\right)^2, \quad (4)$$

Table 4
CaF Equilibrium Constants in Reciprocal Centimeters (r_e in ångström) for the Ground State $X^2\Sigma^+$ and Two Excited States $A^2\Pi$ and $B^2\Sigma^+$

$X^2\Sigma^+$		
Constants	This Work	Previous Works
ω_e	588.64510(45)	588.644(2)[a], 588.67608(29)[b]
$\omega_e x_e$	2.91253(20)	2.91194(6)[a], 2.91259(12)[b]
$\omega_e y_e$	0.008531(34)	0.00841499(4)[a], 0.008514(20)[b]
$10^6\omega_e z_e$	−7.1(19)	−6.1(11)[b]
B_e	0.34371022(56)	0.34370924(4)[a], 0.3437181(12)[b]
α_e	0.00244572(29)	0.00244460(9)[a], 0.002444671(93)[b]
$10^6\gamma_e$	5.287(31)	4.917(20)[b]
$10^7 D_e$	4.68636(55)	4.6879(8)[a], 4.6954(20)[b]
$10^7\beta_e$	0.00238(29)	0.00137(8)[a], 0.00129(11)[b]
$10^7\gamma_e$	−0.000301(31)	−0.000237(12)[b]
$\gamma_{sr,e}$	0.00132343(60)	…
α_γ	−0.00001093(21)	…
r_e	1.9516371(16)	1.9516403(1)[a]

$B^2\Sigma^+$		
Constants	This Work	Previous Works
ω_e	572.40853(83)	572.424(80)[a], 572.405(36)[d]
$\omega_e x_e$	3.14494(12)	3.101(37)[a], 3.143(13)[d]
$\omega_e y_e$	0.0096825(48)	0.0095(15)[d]
B_e	0.3426123(54)	0.342345(10)[a], 0.342604(7)[d]
α_e	0.0026289(12)	0.002577(12)[a], 0.002630(6)[d]
$10^6\gamma_e$	5.839(55)	6.3(4)[d]
$10^7 D_e$	4.9081(84)	4.815(20)[a], 4.66(3)[d]
$10^7\beta_e$	0.0049(15)	0.0393(56)[d]
$\gamma_{sr,e}$	−0.045507(72)	…
α_γ	−0.0003930(73)	…
r_e	1.954762(15)	1.9555(3)[a], 1.955[d]

$A^2\Pi$		
Constants	This Work	Previous Works
ω_e	594.723(74)	594.513(50)[a]
$\omega_e x_e$	3.123(18)	3.031(20)[a]
$\omega_e y_e$	0.0133(16)	…
$\omega_e z_e$	−0.000215(46)	…
B_e	0.348614(24)	0.348781(5)[a], 0.348744(27)[c]
α_e	0.002490(12)	0.002526(6)[a], 0.002529[c]
$10^6\gamma_e$	−4.5(17)	…
$10^6\epsilon_e$	0.400(64)	…
$10^7 D_e$	4.7988(36)	4.8078(3)[a]
$10^7\beta_e$	0.0083(21)	…
A_e	72.6116(91)	71.429(40)[a], 71.475(14)[c]
α_A	0.0303(20)	0.123(4)[a], 0.027(12)[c]
p_e	−0.044232(89)	−0.0438(3)[c]
α_p	−0.000456(52)	…
$10^4 q_e$	−0.000282(18)	…
$10^4\alpha_q$	0.000003(18)	…
r_e	1.937861(66)	1.9374(1)[a]

Notes. One standard deviation is shown in parentheses.
[a] Value from the combined fit of L. A. Kaledin et al. (1999) with deperturbation of A and B states.
[b] From F. Charron et al. (1995).
[c] From J. Nakagawa et al. (1978).
[d] From M. Dulick et al. (1980).

$$p_v = p_e + \alpha_p\left(v + \frac{1}{2}\right) + \gamma_p\left(v + \frac{1}{2}\right)^2, \quad (5)$$

$$q_v = q_e + \alpha_q\left(v + \frac{1}{2}\right), \quad (6)$$

$$\gamma_v = \gamma_{sr,e} + \alpha_\gamma\left(v + \frac{1}{2}\right). \quad (7)$$

The equilibrium bond length r_e was computed from B_e using (P. F. Bernath 2020):

$$r_e(\text{Å}) = \left(\frac{16.857\quad 629\quad 192}{\mu\quad B_e(\text{cm}^{-1})}\right)^{1/2}, \quad (8)$$

with, for $^{40}Ca^{19}F$, the reduced mass $\mu = 12.876740379$ u using the most recent atomic mass evaluation (AME2020) (M. Wang et al. 2021).

The resulting equilibrium constants of all electronic states are presented in Table 4. The available previous literature values with uncertainties are reported. For the ground state, the equilibrium constants calculated by L. A. Kaledin et al. (1999) and F. Charron et al. (1995) are in good agreement. For the $B^2\Sigma^+$ states, the values from this work are in good agreement with the values from M. Dulick et al. (1980) but are slightly different from those of L. A. Kaledin et al. (1999). This is because L. A. Kaledin et al. (1999) considered explicitly the distant perturbation between $B^2\Sigma^+$ and $A^2\Pi$ states in the Hamiltonian. In our work, the perturbation is absorbed into the values of our effective constants for the Λ-doubling parameters and the spin rotation parameters (for example). For the $A^2\Pi$ state, differences with L. A. Kaledin et al. (1999) values exist for the same reason. Also, the value of the spin–orbit constant reported by J. Nakagawa et al. (1978) (71.475 cm^{-1}) is lower than the one found in this work (72.6116 cm^{-1}). This is also due to different Hamiltonians used and specifically a different parameterization of the perturbation of $A^2\Pi$ by distant $^2\Sigma^+$ states: J. Nakagawa et al. (1978) used a parameter o with a large value in addition to p and q. In this work, the effect of o is absorbed in other constants.

3.3. Line Intensity

The line strengths were calculated using PGOPHER from band strengths $<v'|\mu|v''>$. The first step to obtain the band strengths of the A–X and B–X systems is to determine the Rydberg–Klein–Rees (RKR) potential energy surfaces of all three electronic states using equilibrium constants from Equations (1) and (2). This was performed by use of the program written by R. J. Le Roy (2017a). The second step is to use the RKR potential energy surfaces in the LEVEL program (R. J. Le Roy 2017b) in order to solve the 1D Schrodinger equation and obtain vibrational wave functions. Finally, the use of cubic spline interpolated TDM curves $\mu(r)$

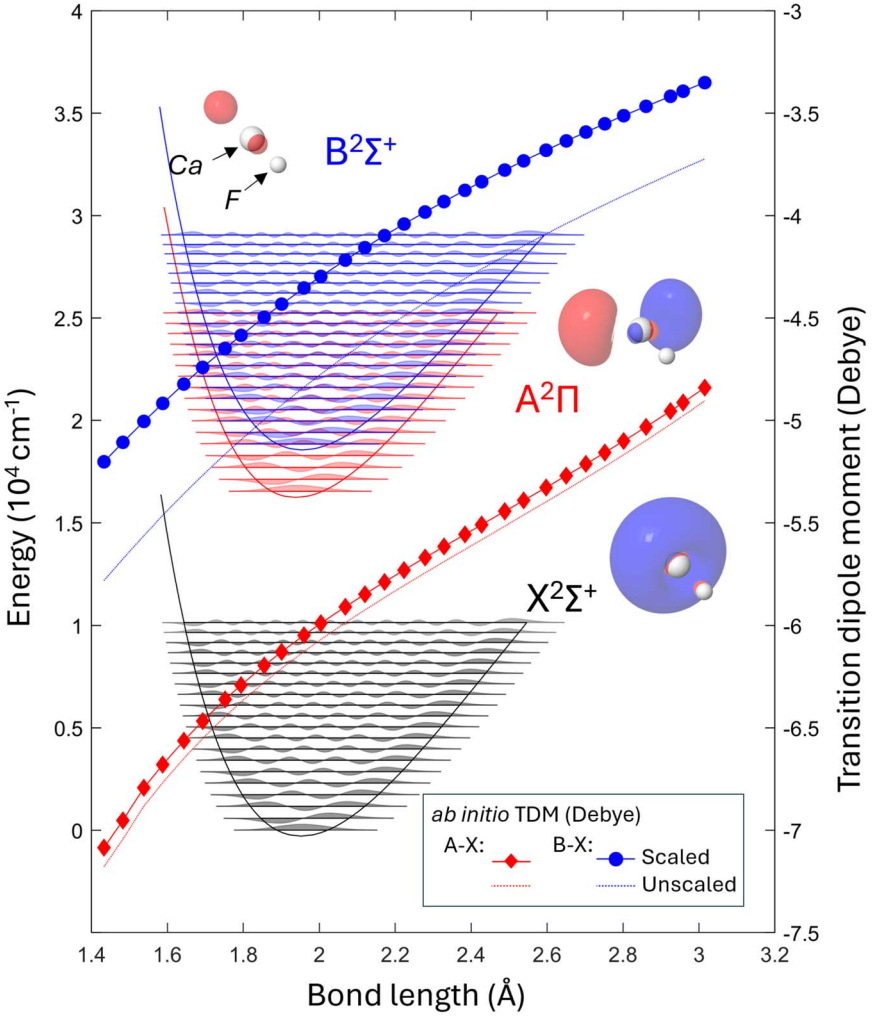

Figure 4. RKR potential energy surfaces (right vertical scale) for $X^2\Sigma^+$ (black), $A^2\Pi$ (red), and $B^2\Sigma^+$ (blue) superimposed with the LEVEL calculated vibrational wave functions. The ab initio TDM calculated in MRCI for *A*–*X* (red) and *B*–*X* (blue) is shown (left vertical scale) as a function of bond length. Electronic states are illustrated with the orbital of the unpaired electron in the main configuration.

allows LEVEL to calculate the band strengths simply as integrals over the bond length r: $<v'|\mu(r)|v''>$.

The TDM curves for *A*–*X* and *B*–*X* were obtained from ab initio calculations (MRCI, see Section 2) and scaled according to the observed lifetimes. The available experimental lifetimes are 19.2 ± 0.7 ns for the $A(v = 0)$ state (T. E. Wall et al. 2008) and 25.1 ± 4 ns for the $B(v = 0)$ state (P. J. Dagdigian et al. 1974). The lifetimes of vibronic states can be obtained from our results. The Einstein *A* coefficients are calculated from band strengths for individual vibrational bands, and then, for a particular vibronic excited state, the lifetime is given by the reciprocal of the sum of all the Einstein *A* coefficients connecting the excited state to lower states. The sum converges rapidly since Einstein *A* coefficients are very small for nondiagonal bands. For the LEVEL lifetime to match the experiment, scalings of 0.987 for the *A*–*X* TDM and 0.900 for the *B*–*X* TDM were necessary. Without scaling, the obtained lifetimes are 18.70 ns for the $A^2\Pi(v = 0)$ state and 20.38 ns for the $B^2\Sigma^+(v = 0)$ state. A relatively large scaling of the *B*–*X* TDM seems to be necessary. A theoretical lifetime for $B(v = 0)$ reported in the literature (19.7 ns; Y. Hao et al. 2019) also shows a significant difference compared to the experiment. P. J. Dagdigian et al. (1974)'s experimental lifetime might be overestimated; in fact, the uncertainty in the reported value is large (4 ns). However, it cannot be excluded that the active space used for ab initio calculations does not capture enough correlation.

The RKR potential energy surfaces and the vibrational wave functions obtained from LEVEL are shown in Figure 4. The scaled and unscaled TDM curves of *A*–*X* and *B*–*X* transitions calculated by ab initio methods (MRCI) are shown with a separate y-scale. The band strengths and Franck–Condon Factors (FCF) of all observed bands obtained using LEVEL and scaled TDM curves are gathered in Table 5. The FCF for the *A*–*X*(0,0) transition was measured using laser-induced fluorescence (T. E. Wall et al. 2008) to be 0.987 and agrees with our value of 0.979 within experimental uncertainties. Similarly, the FCF of *A*–*X*(0,1) and *A*–*X*(0,2) transitions are measured to be 0.03 and 0.0008, respectively, (V. Zhelyazkova et al. 2014) compared to 0.02 and 0.0007 in this work.

Finally, band strengths are used in PGOPHER to calculate the Einstein *A* coefficients of individual ro-vibronic transitions. These are converted to oscillator strengths $f_{J'\leftarrow J''}$ (P. F. Bernath 2020) using

$$f_{J'\leftarrow J''} = \frac{1.499194}{\tilde{\nu}^2}\frac{2J'+1}{2J''+1}A_{J'\rightarrow J''} \quad (9)$$

with $\tilde{\nu}$ in reciprocal centimeters.

Table 5
Band Strengths $<v'|\mu|v''>$ and Franck–Condon Factors (FCF) Calculated Using LEVEL

	$A^2\Pi$–$X^2\Sigma^+$						$B^2\Sigma^+$–$X^2\Sigma^+$					
	$<v'\|\mu\|v''>$ (Debye)			FCF			$<v'\|\mu\|v''>$ (Debye)			FCF		
$v'\Delta v$	−1	0	+1	−1	0	+1	−1	0	+1	−1	0	+1
0	0.9276	−5.9985	…	0.0204	0.9789	…	−0.0960	−4.3539	…	0.0013	0.9986	…
1	1.2765	−5.8617	−0.8159	0.0386	0.9383	0.0211	−0.1563	−4.3350	0.2216	0.0032	0.9953	0.0014
2	1.5195	−5.7298	−1.1410	0.0548	0.8999	0.0413	−0.2163	−4.3134	0.3355	0.0056	0.9907	0.0033
3	1.7036	−5.6033	−1.3804	0.0690	0.8640	0.0607	−0.2781	−4.2887	0.4378	0.0088	0.9846	0.0059
4	1.8479	−5.4828	−1.5731	0.0813	0.8306	0.0791	−0.3422	−4.2607	0.5366	0.0126	0.9770	0.0094
5	1.9625	−5.3686	−1.7344	0.0918	0.7996	0.0966	−0.4084	−4.2289	0.6345	0.0172	0.9675	0.0137
6	2.0540	−5.2609	−1.8723	0.1006	0.7711	0.1130	−0.4768	−4.1931	0.7326	0.0226	0.9562	0.0190
7	2.1269	−5.1596	−1.9918	0.1079	0.7449	0.1285	−0.5470	−4.1530	0.8313	0.0289	0.9429	0.0253
8	2.1843	−5.0647	−2.0962	0.1138	0.7209	0.1429	−0.6189	−4.1082	0.9309	0.0361	0.9274	0.0327
9	2.2289	−4.9761	−2.1880	0.1185	0.6990	0.1564	−0.6920	−4.0584	1.0314	0.0441	0.9096	0.0414
10	2.2625	−4.8935	−2.2691	0.1221	0.6792	0.1690	−0.7660	−4.0034	1.1324	0.0531	0.8895	0.0513
11	2.2869	−4.8164	−2.3410	0.1247	0.6611	0.1808	−0.8408	−3.9429	1.2338	0.0630	0.8670	0.0624
12	2.3032	−4.7447	−2.4051	0.1264	0.6446	0.1917	−0.9158	−3.8766	1.3353	0.0737	0.8420	0.0748
13	2.3125	−4.6777	−2.4623	0.1273	0.6297	0.2020	−0.9907	−3.8043	1.4364	0.0853	0.8146	0.0885
14	2.3153	−4.6152	−2.5138	0.1274	0.6161	0.2115	−1.0652	−3.7257	1.5368	0.0976	0.7848	0.1033
15	2.3111	−4.5572	−2.5600	0.1267	0.6039	0.2205	−1.1388	−3.6408	1.6359	0.1107	0.7526	0.1194
16	2.2973	−4.5049	−2.6008	0.1249	0.5933	0.2287	−1.2111	−3.5494	1.7333	0.1243	0.7182	0.1365
17	…	…	…	…	…	…	−1.2817	−3.4514	1.8284	0.1384	0.6817	0.1544
18	…	…	…	…	…	…	−1.3502	−3.3470	1.9204	0.1528	0.6433	0.1732
19	…	…	…	…	…	…	…	−3.2366	2.0084	…	0.6035	0.1923
20	…	…	…	…	…	…	…	…	2.0905	…	…	0.2114

Note. The values shown here correspond to the experimentally observed bands, $\Delta v = v' - v''$.

Table 6
Sample of the Line List of the $A^2\Pi$–$X^2\Sigma^+$ and the $B^2\Sigma^+$–$X^2\Sigma^+$ Band Systems of CaF

J'	p'	J''	p''	Position cm^{-1}	E_{upper} cm^{-1}	E_{lower} cm^{-1}	A s^{-1}	f	Branch	Label
79.5	f	80.5	f	15865.81119	18686.55039	2820.73921	7.909E+04	4.652E-04	oP12(80.5)	A $v=0$ 79.5 79 F1f–X $v=1$ 80.5 81 F2f
80.5	f	81.5	f	15865.81342	18741.28627	2875.47284	7.822E+04	4.602E-04	oP12(81.5)	A $v=0$ 80.5 80 F1f–X $v=1$ 81.5 82 F2f
78.5	f	79.5	f	15865.82323	18632.47151	2766.64828	7.996E+04	4.703E-04	oP12(79.5)	A $v=0$ 78.5 78 F1f–X $v=1$ 79.5 80 F2f
81.5	f	82.5	f	15865.82996	18796.67823	2930.84827	7.737E+04	4.553E-04	oP12(82.5)	A $v=0$ 81.5 81 F1f–X $v=1$ 82.5 83 F2f
77.5	f	78.5	f	15865.84952	18579.05051	2713.20099	8.085E+04	4.754E-04	oP12(78.5)	A $v=0$ 77.5 77 F1f–X $v=1$ 78.5 79 F2f
82.5	f	83.5	f	15865.86081	18852.72537	2986.86455	7.654E+04	4.504E-04	oP12(83.5)	A $v=0$ 82.5 82 F1f–X $v=1$ 83.5 84 F2f

Note. J' and J'' are the upper and lower state total angular momentum quantum numbers, respectively; p' and p'' are the upper and lower state parity, respectively; the calculated line position is given in reciprocal centimeters; E_{upper} and E_{lower} are the upper and lower energy levels in reciprocal centimeters; A is the Einstein $A_{J'\rightarrow J''}$ value in reciprocal seconds; f is the oscillator strength; and branch/line assignments are the associated quantum numbers for the given transition (see Table 1 for a detailed description).

(This table is available in its entirety in machine-readable form in the online article.)

The line list of the $A^2\Pi$–$X^2\Sigma^+$ and the $B^2\Sigma^+$–$X^2\Sigma^+$ band systems is shown in Table 6. This line list does not contain the unresolved hyperfine structure. The quantity $\log_{10}(gf_{J'\leftarrow J''})$ can be derived for individual transitions by taking the statistical weight g to be $2J'' + 1$.

4. Discussion

The CaCl spectrum was previously investigated using similar methods (L. Lavy & P. F. Bernath 2024). These two systems (CaCl, CaF) are interesting to compare as they are two different calcium monohalide molecules. The most obvious difference is the mass of the fluorine atom, which is lighter than chlorine. As a result, the CaF B_e constant is larger and the equilibrium bond length shorter. CaF and CaCl electronic structures are similar: they both have low-lying excited states $A^2\Pi$ and $B^2\Sigma^+$, and a $X^2\Sigma^+$ ground state. The origin (T_v) and spin–orbit coupling (A_e) of the A state have the same magnitude in both molecules and the band heads in the A–X transition are blue-degraded.

While the $\Delta v = 0$ sequence is very similar in both molecules, CaF distinguishes itself in the $\Delta v = +1$ sequence as it has no band heads in the $\Omega = 1/2$ spin component. The CaF shape of $\Delta v = -1$ sequence is also different because the two spin components are not clearly distinct, in contrast with CaCl. The second excited state $B^2\Sigma^+$ is distant by ~2300 cm^{-1} relative to $A^2\Pi$ in CaF whereas it is only ~700 cm^{-1} away for CaCl. The B–X systems are radically different, mainly because

in CaF the rotational constant of the B state has a lower value than that in the ground state. In CaF, the prominent band heads are in the R branch (red-degraded) and, because the band origin decreases with vibrational quantum number, the vibrational bands are heavily overlapping. In CaCl, the band origin also decreases with vibrational quantum number, however, since the prominent band heads are in the P branch (blue-degraded), the vibrational bands are sharply separated.

The TDMs of A–X and B–X transitions have the same order of magnitude for both CaCl and CaF; however, they differ slightly in their bond length dependence. Diagonal band strengths for the A–X system are similar, but the band strengths for the B–X system of CaCl drop very rapidly with the vibrational quantum number v compared to the band strengths of CaF that stay strong up to high v. The CaF spectrum shows significant strength for high vibrational quantum numbers, whereas in CaCl the strongest bands are those with the lowest vibrational quantum numbers.

In stellar spectroscopy the identification of molecules can be difficult because of overlapping bands. The A–X $\Delta v = 0$ sequence of CaF overlaps with A–X $\Delta v = +1$ and B–X $\Delta v = -1$ sequences of CaCl. The strongest CaF A–X bands do not overlap with the strong VO and TiO bands expected in M-type stars; however, they overlap significantly with the strongest features of the ScO A–X transition. CaF might also be masked by ZrO and CrO bands. However, the features of CaF and CaCl are expected to be very distinct; their band systems are very compact and their band heads are blue-degraded (for the A–X band system) as opposed to all of the cited metal oxides. For detection in C-type stars, the A–X feature of CaF does not overlap with the strongest features of C_2 and CN. It is interesting to note that M. Agúndez et al. (2020) predicted a strong presence of CaCl in M-type stars while it has been observed only in S-type and C-type stars so far, probably because of the aforementioned overlapping bands. For the same reason, the CaF molecule should be searched for in S- and C-type stars. Alternatively, the recently published line list of ScO (L. Lavy et al. 2024) can be used to deconvolve overlapping molecular bands in M-type stars.

5. Conclusion

In this study, a Doppler-limited spectrum of CaF was obtained with the use of a Fourier transform spectrometer and a hollow cathode source. A fit to obtain spectroscopic constants was made in two steps: first, the ground state $X^2\Sigma^+$ of CaF was fitted using infrared, microwave, and radio lines from the literature (W. Childs et al. 1981; G. Weiler 1986; M. A. Anderson et al. 1994; F. Charron et al. 1995). Then, the excited states $A^2\Pi$ and $B^2\Sigma^+$ were fitted using lines from R. W. Field et al. (1975), J. Nakagawa et al. (1978), M. Dulick et al. (1980), L. A. Kaledin et al. (1999), as well as lines and band heads assigned in this work belonging to the $A^2\Pi$–$X^2\Sigma^+$ and the $B^2\Sigma^+$–$X^2\Sigma^+$ band systems. Although no individual lines could be observed for $v' > 4$ in the present study, the use of band head positions constrained some parameters and gives a coherent and complete simulation of the observed spectrum. Constants for $A^2\Pi$ with $v' \leqslant 16$ and for $B^2\Sigma^+$ with $v' \leqslant 20$ are therefore presented. With a fitted vibrational temperature of 4000 K, our analysis is well suited for the analysis of spectra of AGB atmospheres.

The equilibrium constants of the electronic states of CaF were calculated and compared to the literature. In general, our results agree well with the literature; however, the perturbation of $A^2\Pi$ by distant $^2\Sigma^+$ states was not explicitly taken into account in our study. This produces no loss in the empirical description and explains the discrepancy between some equilibrium constants from this work and previous works. We calculated TDM curves for the two electronic transitions that agree with previous calculations from the literature. We corrected our calculations using experimental lifetimes. The band strengths obtained with corrected TDM reproduce the observed intensities in the hollow cathode spectrum satisfactorily. Using the corrected TDM, we calculate Einstein A and oscillator strengths of individual lines and provide those in the form of a line list.

The line list can be used for the detection of CaF in stellar atmospheres. Strong TiO and VO signals should not compromise CaF detection; however, the overlap with ScO might mask the strongest CaF band in M-type stars. Such a limitation does not exist in C-type stars, where the strong C_2 and CN features do not overlap with CaF.

Acknowledgments

Financial support was provided by the NASA Laboratory Astrophysics Program (80NSSC21K1463, 80NSSC24K1750). P.B. acknowledges R.B. for productive discussion.

Data Availability

The tabular data (Tables 1, 2, 6) created for this work is provided in the machine-readable format in the online Journal article. The PGOPHER (Version 10.1.182) configuration file, containing the published spectroscopic constants and band strengths, is available on Zenodo doi:10.5281/zenodo.14080064.

ORCID iDs

Léo Lavy https://orcid.org/0000-0003-4572-8612
Peter F Bernath https://orcid.org/0000-0002-1255-396X
Adam Pastorek https://orcid.org/0000-0001-7935-8571

References

Agúndez, M., Martnez, J. I., de Andres, P. L., Cernicharo, J., & Martn-Gago, J. A. 2020, A&A, 637, A59
Anderson, M. A., Allen, M. D., & Ziurys, L. M. 1994, ApJ, 424, 503
Asplund, M., Grevesse, N., Sauval, A. J., & Scott, P. 2009, ARA&A, 47, 481
Bernath, P., Cummins, P., & Field, R. 1980, CPL, 70, 618
Bernath, P. F. 2020, Spectra of Atoms and Molecules (4th ed.; Oxford: Oxford Univ. Press)
Brown, J. M., & Carrington, A. 2003, Rotational Spectroscopy of Diatomic Molecules (Cambridge: Cambridge Univ. Press)
Charron, F., Guo, B., Zhang, K., Morbi, Z., & Bernath, P. 1995, JMoSp, 171, 160
Childs, W., Goodman, G., & Goodman, L. 1981, JMoSp, 86, 365
Clegg, R., & Wyckoff, S. 1977, MNRAS, 179, 417
Dagdigian, P. J., Cruse, H. W., & Zare, R. N. 1974, JChPh, 60, 2330
Dulick, M., Bernath, P. F., & Field, R. W. 1980, CaJPh, 59, 703
Field, R. W., Harris, D. O., & Tanaka, T. 1975, JMoSp, 57, 107
Gerstenkorn, S., & Luc, P. 1979, RvPA, 14, 791
Gupta, H., Changala, P. B., Cernicharo, J., et al. 2024, ApJL, 966, L28
Hao, Y., Pateka, L. F., Visscher, L., et al. 2019, JChPh, 151, 034302
Hill, J. G., & Peterson, K. A. 2017, JChPh, 147, 244106
Hou, S., & Bernath, P. F. 2018, JQSRT, 210, 44
Jorissen, A., Smith, V., & Lambert, D. 1992, A&A, 261, 164
Kaledin, L. A., Bloch, J. C., McCarthy, M. C., & Field, R. W. 1999, JMoSp, 197, 289
Kendall, R. A., Dunning, T. H., & Harrison, R. J. 1992, JChPh, 96, 6796
Kreplin, D. A., Knowles, P. J., & Werner, H.-J. 2019, JChPh, 150, 194106
Lavy, L., & Bernath, P. F. 2024, ApJ, 970, 13

Lavy, L., Pastorek, A., & Bernath, P. F. 2024, ApJ, 975, 180
Le Roy, R. J. 2017a, JQSRT, 186, 158
Le Roy, R. J. 2017b, JQSRT, 186, 167
Learner, R. C. M., & Thorne, A. P. 1988, JOSAB, 5, 2045
Luo, Y.-R. 2007, Comprehensive Handbook of Chemical Bond Energies (Boca Raton, FL: CRC Press)
Nakagawa, J., Domaille, P. J., Steimle, T. C., & Harris, D. O. 1978, JMoSp, 70, 374
Owens, A., Mitrushchenkov, A., Yurchenko, S. N., & Tennyson, J. 2022, MNRAS, 516, 3995
Pelegrini, M., Vivacqua, C. S., Roberto-Neto, O., Ornellas, F. R., & Machado, F. B. C. 2005, BrJPh, 35, 950
Rajpurohit, A. S., Reyl, C., Allard, F., et al. 2013, A&A, 556, A15
Rumble, J. 2023, CRC Handbook of Chemistry and Physics (104th ed.; London: Taylor and Francis)
Saberi, M., Khouri, T., Velilla-Prieto, L., et al. 2022, A&A, 663, A54
Skidmore, W. 2015, RAA, 15, 1945
Tennyson, J., & Yurchenko, S. N. 2012, MNRAS, 425, 21
Wall, T. E., Kanem, J. F., Hudson, J. J., et al. 2008, PhRvA, 78, 062509
Wang, M., Huang, W., Kondev, F., Audi, G., & Naimi, S. 2021, ChPhC, 45, 030003
Weiler, G. 1986, PhD thesis, Freie Univ. Berlin
Werner, H., Knowles, P. J., Knizia, G., Manby, F. R., & Schütz, M. 2011, WIREs Computational Molecular Science, 2, 242
Werner, H.-J., & Knowles, P. J. 1985, JChPh, 82, 5053
Werner, H.-J., & Knowles, P. J. 1988, JChPh, 89, 5803
Werner, H.-J., Knowles, P. J., & Knizia, G., 2022 MOLPRO v2012.1, A Package of Ab Initio Programs, https://www.molpro.net
Werner, H.-J., Knowles, P. J., Manby, F. R., et al. 2020, JChPh, 152, 144107
Werner, K., Rauch, T., & Kruk, J. W. 2005, A&A, 433, 641
Western, C. M. 2017, JQSRT, 186, 221
Whaling, W., Anderson, W., Carle, M., Brault, J., & Zarem, H. 1995, JQSRT, 53, 122
Zhelyazkova, V., Cournol, A., Wall, T. E., et al. 2014, PhRvA, 89, 053416
Ziurys, L. M., Apponi, A. J., & Phillips, T. G. 1994, ApJ, 433, 729